CHAPTER 5

Synthesis and photocatalytic applications of starch functionalized α-FeOOH/β-FeOOH nanocomposites

5.1 Introduction

Phenolic waste and organic dyes are significant organic pollutants of industrial wastewater because of their high toxicity and persistence. Para-nitrophenol (PNP) and methyl orange (MO) are two representatives of these classes of industrial chemicals. The synthesis of different pesticides, insecticides, herbicides, explosives, synthetic dyes, and pharmaceuticals involves PNP. It is also a toxic, persistent, bioaccumulative, non-biodegradable, and potentially carcinogenic chemical. MO is an industrial azo dye with wide use in textiles, foodstuffs, paper, and leather industries. Both substances can enter the natural environment in the form of industrial effluents and pose a severe risk to the ecosystem and human health [Arslan *et al.* (1999), Environmental Protection Agency (2000), Sun and Lemley *et al.* (2011)]. Indeed, effluents containing these wastes should be treated effectively before their discharge in natural aquatic reservoirs.

Scientific literature mentions a large number of methods for the removal or degradation of these chemicals from industrial effluents [Peretti *et al.* (2001), Robinson *et al.* (2001), Luan and Plaisier *et al.* (2004), Devi *et al.* (2009), Chen *et al.* (2016), Li *et al.* (2016), Xie *et al.* (2016), Zhou *et al.* (2016)]. Among these, heterogeneous Fenton and photo-Fenton like advanced oxidation techniques (AOP) [Nidheesh *et al.* (2015)] can oxidatively degrade PNP and MO into environmentally benign products. In heterogeneous Fenton processes, catalyst recycling is possible, and unlike conventional Fenton methods, there is no sludge formation [Pereira *et al.* (2012)].

Sun *et al.* (2011) were perhaps the first to report the heterogeneous Fenton-like AOP degradation with H_2O_2 of PNP using commercially manufactured nanoparticles of magnetite (Fe_3O_4). They found it took about 10 hours to degrade almost all of PNP under the reported Fenton experimental conditions. The degradation pathway involved the formation of benzoquinone, hydroquinone, 1,2,4-trihydroxy benzene, and p-nitrocatechol

intermediates. Later, hydroxyl radicals also degraded these intermediates. Natural magnetite is also a heterogeneous catalyst for PNP's Fenton degradation [Hongping *et al.* (2015)]. Maghemite nanostructures loaded on SiO_2 have also been used for this purpose [Ferroudj *et al.* (2013)]. The effect of functionalization of iron oxides/oxyhydroxides on their Fenton reactivity is another exciting feature. Thus, Hou *et al.* reported that hydroxylamine functionalized goethite shows enhanced Fenton catalytic activity towards many dyes, pesticides, and antibiotics [Hou *et al.*, 2017]. These authors proposed that electron transfer from hydroxylamine to Fe (III) converts it into Fe (II) species on the surface of the catalyst to increase its H_2O_2 reduction activity. Hence, features favorable for photocatalytic properties of such iron oxide/oxyhydroxides can further improve their heterogeneous Fenton activity.

Iron oxide/oxyhydroxide phases, with their band gaps in the 2.0-2.9eV range, have exhibited visible light photocatalytic properties for various reactions. Among these, maghemite suffers from photo dissolution [(Zhang *et al.* (2011), Kakuta *et al.* (2014), Mamba and Mishra *et al.* (2016)], while there are reports in the literature on the effectiveness of goethite and akageneite nanoparticles as visible light photocatalysts. For instance, Jelle *et al.* (2016) proposed that photoexcited holes were responsible for generating highly reactive hydroxyl radicals for the photocatalytic degradation of methylene blue by both pure goethite and akageneite nanoparticles under aerobic conditions.

Here it must be mentioned that there are no reports on photo-Fenton degradation of PNP by either goethite or akageneite nanoparticles. Though, there are a few studies on photo Fenton degradation of PNP catalyzed by other nanomaterials. Like, Fe-doped TiO_2 was used by Zhao *et al.* (2010) for photo-Fenton PNP degradation, but this photocatalyst was only effective under UV radiation. Recently, visible light photo-Fenton degradation

of PNP on graphitic carbon nitride supported iron oxide nanocomposites has also been reported [Lin *et al.* (2017)]. The mechanism proposed by the authors postulated the photo-reduction of H_2O_2 to hydroxyl radicals, which then oxidize PNP. To date, there are very few reports in the literature on the use of nanocomposites consisting of two or more iron oxide/oxyhydroxide phases as photocatalysts for photo-Fenton organic contaminant degradation.

Nanomaterials made up of pure iron oxide/oxyhydroxide phase alone have relatively weaker photocatalytic activity because of rapid recombination and low photo-absorption coefficient. The bandgap of goethite and akageneite nanoparticles varies in the 2.0 to 2.9 eV range [Zhang *et al.* (2011)]. Therefore, a combination of such iron oxyhydroxide phases with other materials with visible range band gaps should result in better charge separation. The necessary condition is that the band alignment of component iron oxide or oxyhydroxide phases should be staggered for efficient charge separation. Another advantage of using such composite materials is that many of these oxides (especially goethite (α-FeOOH) and hematite (α-Fe_2O_3)) are extremely common in soils and sediments [Singh *et al.* (2017), Qian *et al.* (2018)].

This chapter presents the synthesis of nanocomposites of goethite and akageneite given the preceding discussion. Both phases have band gaps in the visible range. Goethite is an n-type semiconductor, while akageneite is a p-type [Sun *et al.* (2018), Malathi *et al.* (2018), Zheng *et al.* (2016)]. The present study demonstrates that such nanocomposites involve p-n junctions and are efficient visible-light photocatalysts for photo-Fenton degradation of PNP and MO. Compared to the heterogeneous Fenton activities in the dark, the catalytic activity got enhanced under visible light irradiation. Additionally, these nanocomposites were also prepared with and without water-soluble starch, giving access to different catalytic and adsorption properties. The stabilizing agent could alter the shape

and size of the prepared nanocomposites. The preference for water-soluble starch was because it being an economical, biocompatible, biodegradable natural polymer. In the rest of this chapter, starch functionalized and non-functionalized iron hydroxides nanocomposites are abbreviated as S2 and S1, respectively. Starch improved the size distribution, aqueous dispersibility, and stability of these nanoparticles [Bajpai and Likhitkar *et al.* (2013)]. Besides this, the results show that starch functionalization alters the photocatalyst's band structure, making it more efficient.

5.2 Experimental Methods

5.2.1 Synthesis of S1 and S2 nanocomposites

All chemicals used in synthesis were of analytical grade. The following green co-precipitation method was employed to prepare sample S1. Firstly, anhydrous $FeCl_3$ (Merck) was dissolved in an appropriate amount of deionized water. The solution formed was heated at 80-90^oC with mechanical stirring for 15 minutes. At this stage, an appropriate amount of 32M NaOH was added in a dropwise manner. The whole reaction mixture was maintained in the stated temperature range until dark brown precipitate formation was observed. The precipitate was repeatedly washed with deionized water to remove excess NaOH and make it neutral. In the final step, the precipitate was dried in a hot air oven.

For the S2 sample, after preparing the aqueous solution of anhydrous $FeCl_3$, 2wt% freshly prepared aqueous starch (Merck) solution was added while maintaining the reaction mixture temperature within 80-90^oC along with continued stirring. Then the same amount of NaOH (as for the preparation of S1) was added along with heating until complete precipitate formation. The obtained precipitate was repeatedly washed until neutral and dried.

5.2.2 Catalytic degradation of PNP over S1 and S2

For oxidative catalytic degradation investigations over S1 and S2, 50 µL catalyst (1mg in 1mL distilled water) suspension was mixed with 2mL of PNP (0.2mL of 176µM diluted with 2 mL distilled water) solution at pH 3. The pH of the PNP was maintained with the help of 0.1M HCl and 0.1 M NaOH. This suspension was then kept for adsorption (for 60 minutes) until equilibrium. Then, 100µL of 50 mM H_2O_2 (Merck) solution was added to this suspension. Both Fenton and photo-Fenton activities of these nanocomposites were investigated by conducting the PNP degradation in the dark and under (cool white LED) visible light, respectively

5.2.3 Catalytic degradation of MO over S1 and S2

For catalytic degradation of MO over S1 and S2, 50µL of the dispersed catalyst (1mg in 1mL distilled water) was added to 2mL of a 140µM MO solution at pH 3. This suspension was then kept for adsorption (for 60 minutes) until equilibrium. Next, 100µL of 50 mM H_2O_2 solution was added to the reaction mixture. The rest of the procedure was the same as that in the previous sub-section.

5.2.4 Characterization

Powder X-ray Diffraction (XRD) was carried out on a Rigaku Miniflex 600 DTEXULTRA instrument with Cu K_α radiation (λ=1.54 A°) at the scan rate of 10°/min in the range 10-90° of 2θ values. The XRD pattern peaks were assigned to respective crystallographic planes based on data from JCPDS powder diffraction files. The FTIR spectral data were measured on a Varian Excalibur 3100. TEM and HR-TEM imaging were carried out using FEI Technai-20 G^2 200 at the operating voltage of 200 kV. Solid-state UV–vis DRS spectral measurements were performed in the 200–800 nm spectral range. The instrument used for this purpose was the Shimadzu Pharmaspec UV-1700

model, operating. Absorption spectrums (of PNP and MO under photo Fenton conditions) were measured at regular intervals on Agilent Cary 60 UV-visible spectrophotometer.

5.3 Results and Discussion

5.3.1 Characterization of S1 and S2

Figure 5.1 shows the normalized X-ray diffraction (XRD) patterns of S1 and S2 powder samples. The XRD patterns of S1 and S2 display the same peaks. XRD pattern indexing revealed that the peaks were in agreement with the planes of akageneite (JCPDS no 75-1594) and goethite (JCPDS 81-0464) [Mackay *et al.* (1960), Hazemann *et al.* (1991)]. Thus, the phase composition of both S1 and S2 are the same, and hence, starch functionalization does not affect the phase composition.

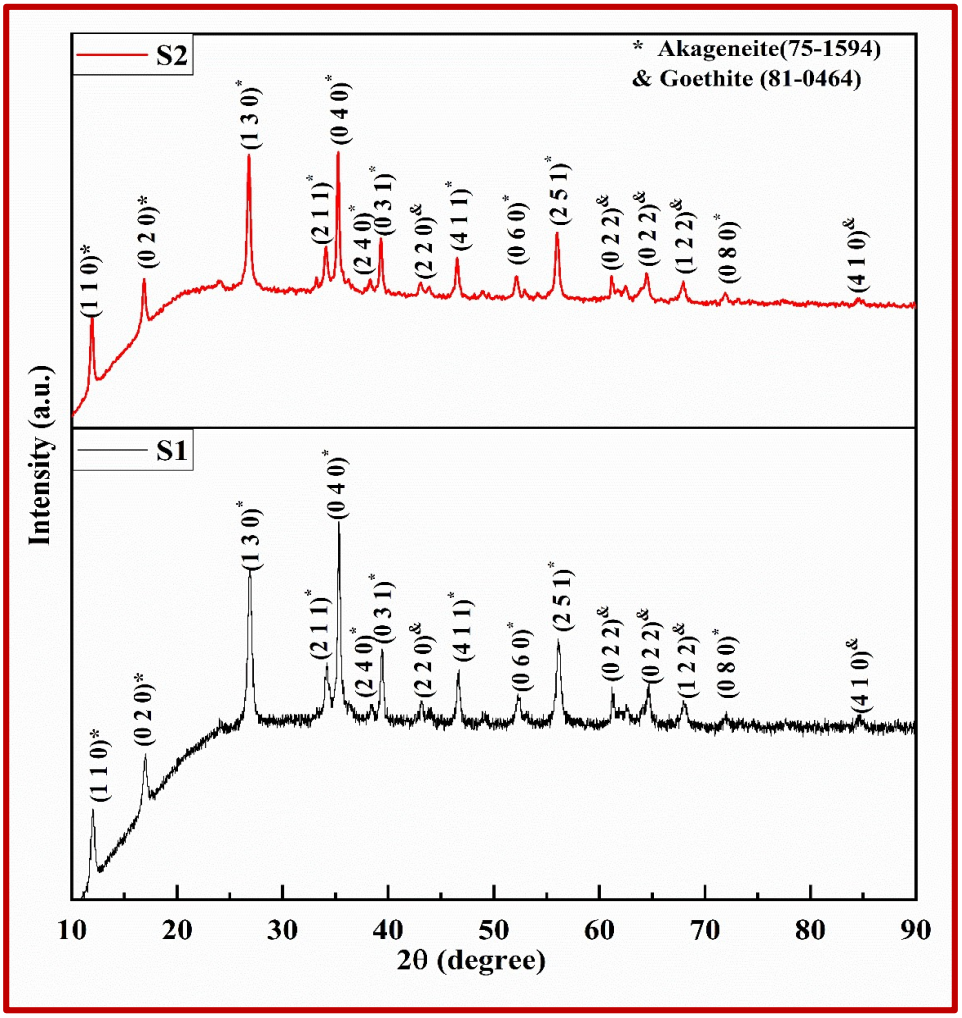

Figure 5.1 The XRD patterns of S2 and S1 powder samples.

Figure 5.2 displays the FTIR spectrums of S2 and S1 samples. For the sake of comparison, this figure also shows the FTIR of soluble starch. The FTIR spectrum of starch shows characteristic peaks at 2926, 1155, and 1023 $cm^{-1,}$ corresponding to stretching frequencies of C-H and glycosidic C-O-C and C-O bonds, respectively. These peaks are there in the FTIR of S2 as well. However, the C-H, C-O-C, and C-O bonds' stretching frequencies are slightly shifted (at 2924, 1150, and 1025 $cm^{-1,}$ respectively) in the FTIR spectrum of S2. As expected, the starch specific frequencies are not present in the FTIR of (the non-starch functionalized) S1 sample. The S1 FTIR spectrum showed absorption at 475 cm^{-1} due to the presence of the Fe-O bond. Starch functionalization slightly blue-shifted this band to 480 cm^{-1} in S2. The peak at ~1638 cm^{-1} appears due to the O-H vibration mode of adsorbed water, and the in-plane bending vibration of O-H of FeOOH causes the absorption at ~1386 cm^{-1} [Bumajdad *et al.* (2011), Hassan *et al.* (2018)]. Two slightly different OH sites seem to be the reason for the stretching bands in the FTIR of S1 at 3488 and 3390 cm^{-1}. Furthermore, the starch modification of S2 red-shifts these two bands. The deformation vibrations of Fe–OH groups resulted in the IR bands at 833 and 695 cm^{-1} in S1, whereas the shoulder at 645 cm^{-1} is due to the interaction of the Fe–OH groups with Cl^- ions [Music *et al.* (2003), Parameshwari *et al.* (2011)]. The FTIR of S2 also shows the stretching and deformation vibration peaks of –OH groups. These peaks appear at slightly shifted positions in FTIR of S2 due to starch functionalization. The simultaneous presence of absorption regions due to both iron oxide and the (C-H, C-O-C, and C-O) stretching modes of the polysaccharide confirmed the starch functionalization of the S2 nanocomposites.

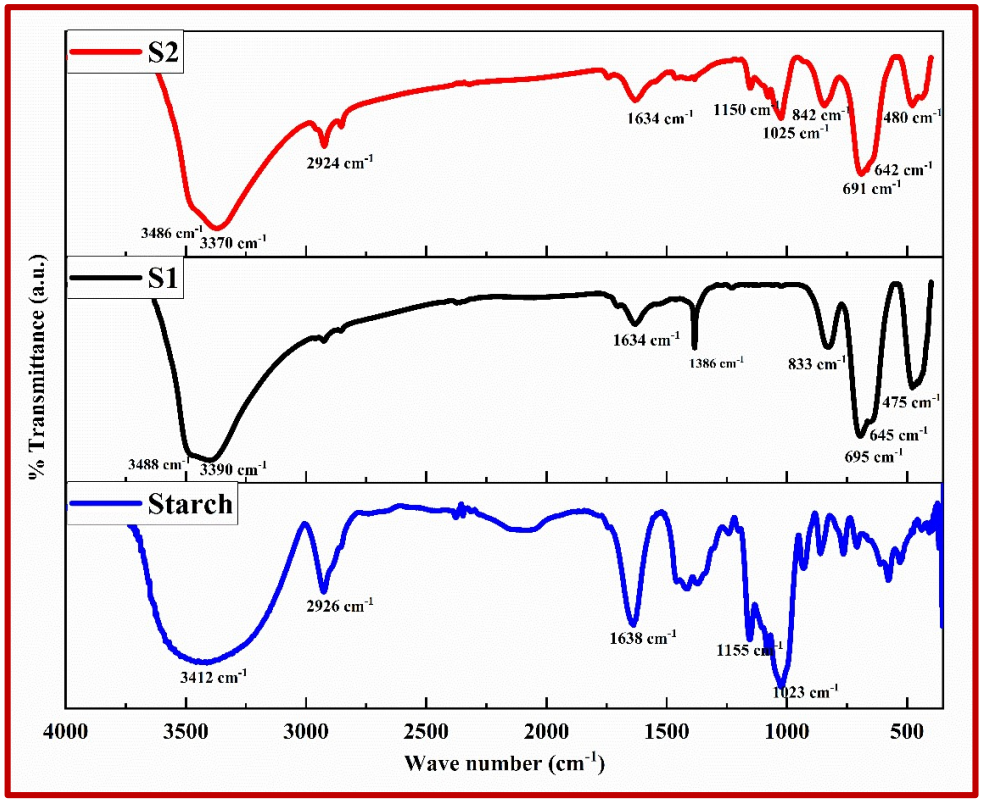

Figure 5.2 A comparison between FTIR plots of soluble starch, S1, and S2 samples.

Figure 5.3 provides the representative TEM images of S1 and S2 samples. In the absence of starch, rod-shaped iron oxyhydroxide nanostructures were obtained (Figure 5.3a). The average length of these rods was 124 nm, and their breadth was 25 nm. Starch functionalization induced the formation of rice-shaped iron oxyhydroxide nanoparticles (Figure 5.3c). The average particle sizes observed in S2 were smaller, both length (98 nm) and breadth (19 nm) wise. In agreement with previous publications, the stabilizer influences the nanostructures' shape and size but not their phase composition [Kango *et al.* (2013)].

Figure 5.3b and 5.3d represent the HRTEM images of S1 and S2, respectively. The fringe spacing of HRTEM of S1, 0.73, and 0.50 nm was indexed to the (1 1 0) and (0 2 0) lattice planes of akageneite (JCPDS: 75-1954) and goethite (JCPDS: 81-0464), respectively. The 0.23 nm and 0.25 nm fringe spacings in S2 were indexed to (2 0 0) and

(2 1 1) lattice planes of goethite (JCPDS: 81-0464) and akageneite (JCPDS: 75-1954), respectively.

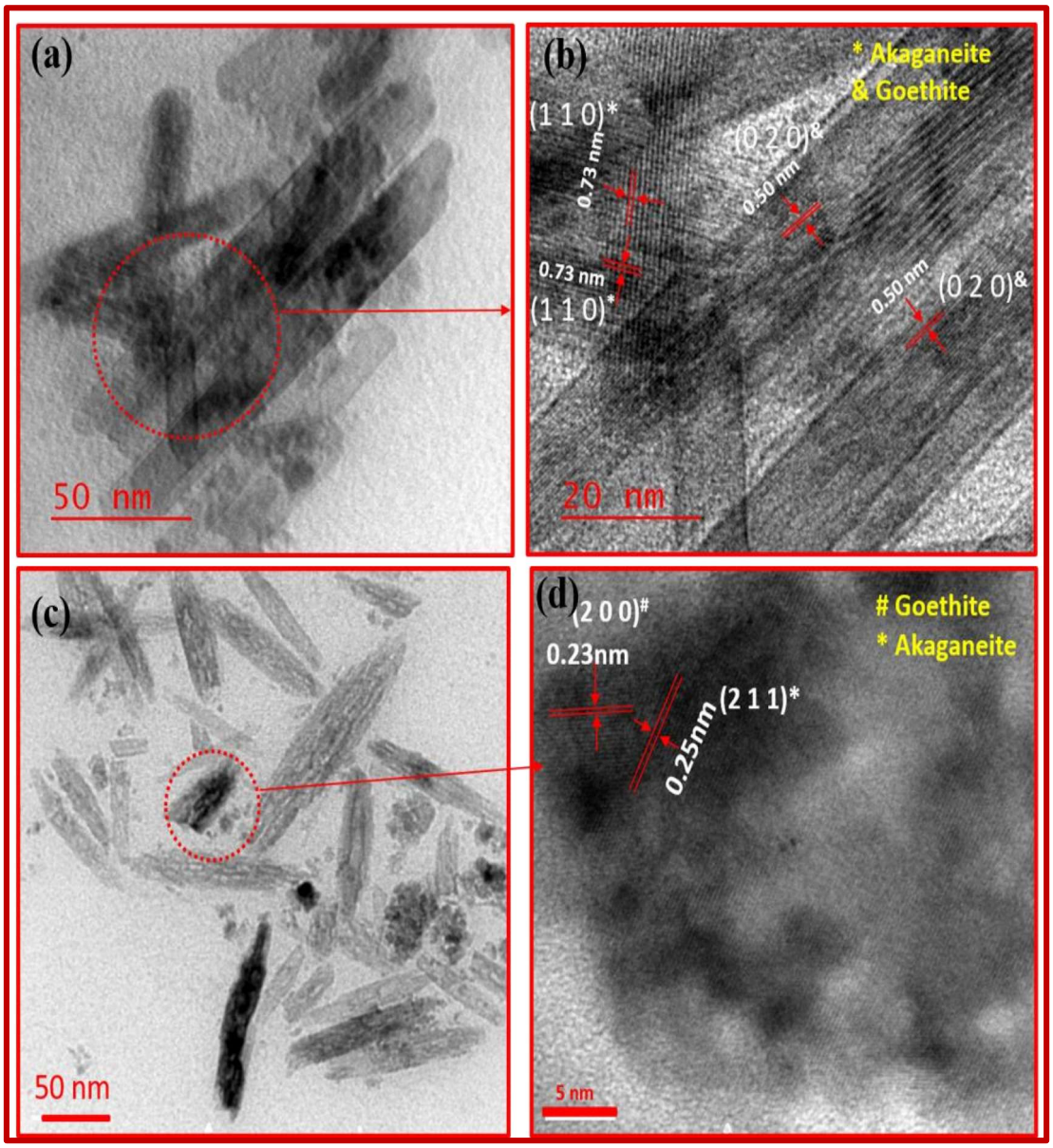

Figure 5.3 TEM images of **(a)** S1 and **(c)** S2. Corresponding HR-TEM images of **(b)** S1 and **(d)** S2.

5.3.2 Optical band gap

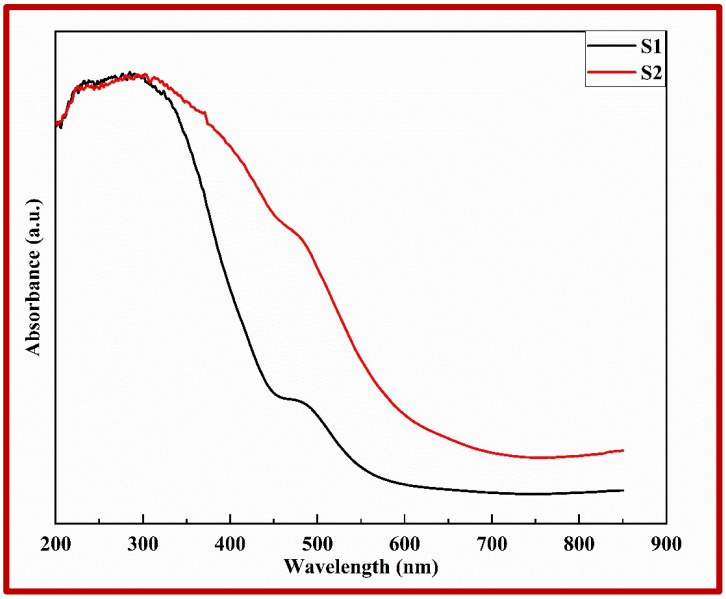

Figure 5.4 Solid-state UV-visible absorption spectra of samples S1 and S2.

Knowing the optical band gaps in the investigated nanomaterial is essential for finding the possible photocatalytic mechanism in operation. Tauc plots from the normalized plots for solid-state UV-vis plots of S1 and S2 (Figure 5.4) helped determine the optical band gaps of S1 and S2. The following equation gives the Tauc relation between the absorption coefficient alpha (α) and photonic energy (hυ):

$$\alpha = \frac{1}{h\upsilon}(h\upsilon - E_g)^n \text{ or } (\alpha h\upsilon)^{1/n} = h\upsilon - E_g \qquad (2.2)$$

In the above equation, α denotes the molar absorption coefficient, n is the transition mode power factor, and Eg is the semiconductor's bandgap energy. The exponent n has a value of 0.5 for allowed direct transition and 2 for indirect transition [Kumar *et al.* (2018)]. Figure 5.5a and 5.5b give the direct transition ($(\alpha h\upsilon)^2$ vs. hυ) Tauc plots for S1 and S2, respectively. The linear fit extrapolated to the (hυ) axis gave the value of optical bandgap energy. The Tauc plots of both S1 and S2 display two bandgaps each.

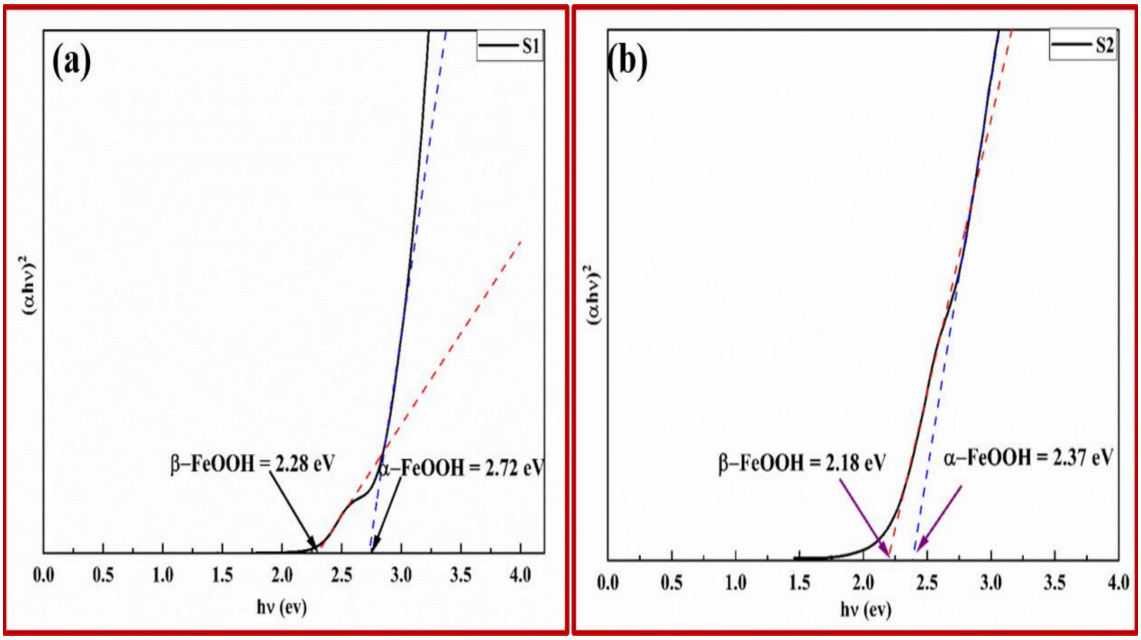

Figure 5.5 Tauc plots of **(a)** S1 and **(b)** S2 (direct transitions).

Sample S1 has two direct band gaps at 2.72 eV and 2.28 eV. These are ascribed to α-FeOOH and β-FeOOH phases, respectively, in S1. In contrast, the respective bandgaps in S2 are 2.37 eV and 2.18 eV. Analogous to S1, the larger bandgap is assigned to α-FeOOH and the smaller one to the β-FeOOH phase. The starch modification reduces the bandgaps of α-FeOOH and β-FeOOH phases. This observation is in agreement with previous reports that organic functionalization of a nanoparticle can alter its band gap [Radoń *et al.*, (2017), Shukla and Sinha *et al.* (2018)].

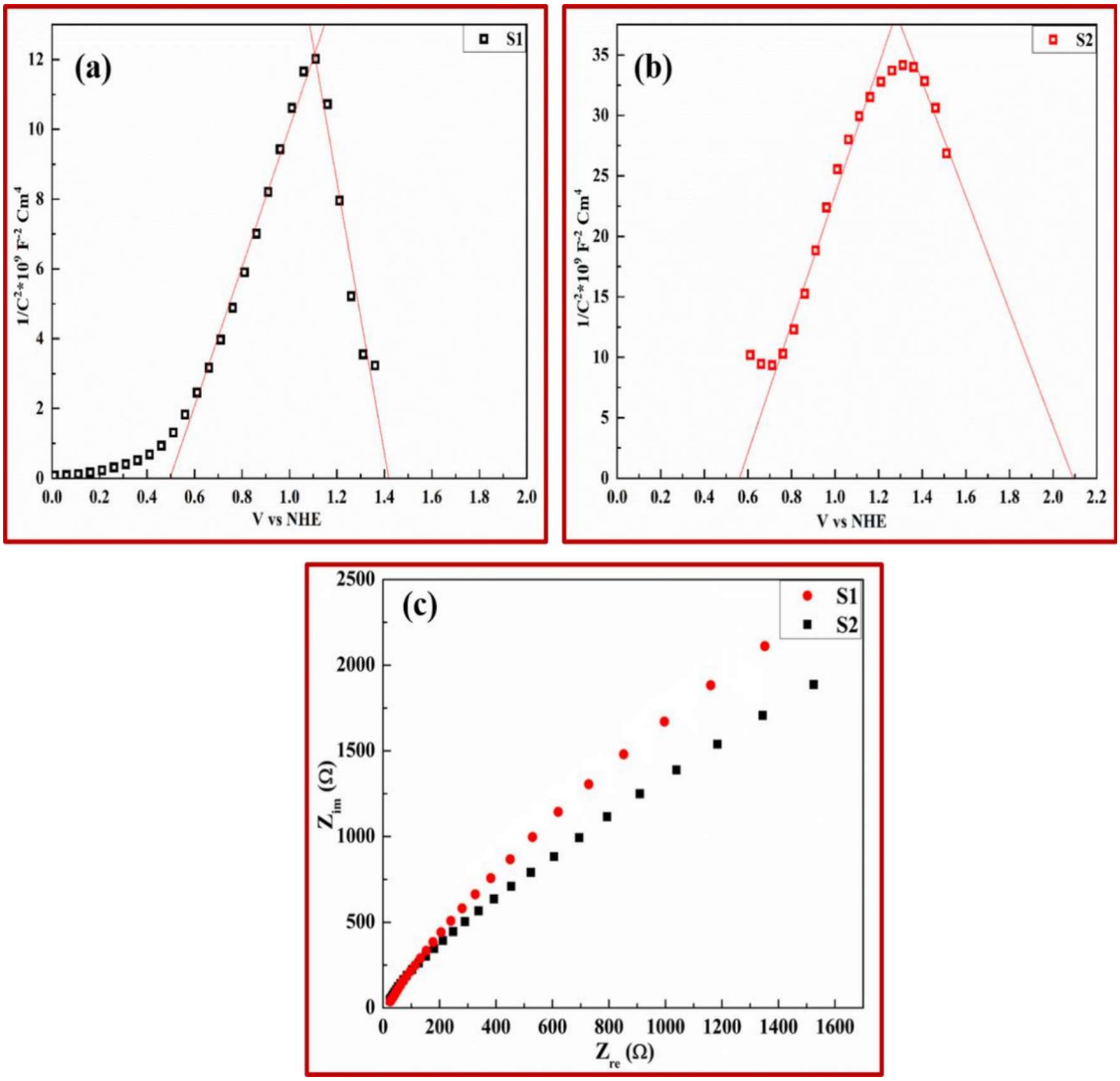

Figure 5.6 Mott Schottky plots of **(a)** S1 and **(b)** S2 measured under the dark condition in 0.5M Na_2SO_4 at 1 kHz. **(c)** The Nyquist EIS plots for S1 and S2 for investigating the electron transfer kinetics of the catalysts.

The flat band potential values for the two components in each nanocomposite were estimated from their Mott–Schottky (MS) plots measured under dark conditions (Figure 5.6). The MS plots (of both S1 and S2) exhibited positive and negative slope parts, confirming a p-n heterojunction. Flat band potential values obtained for S1 were +0.50 eV *vs.* NHE and +1.41 eV *vs.* NHE. The flat band potentials observed for S2 were +0.54 eV *vs*. NHE and + 2.1 eV *vs*. NHE. The potential *vs*. Ag/AgCl reference electrode was converted to the potential *vs*. NHE by the relation

$V(\text{NHE}) = V(\text{Ag/AgCl}) + 0.059\,\text{pH} + 0.197$ (here pH = 7). Figure 5.7 displays the band alignments found for the goethite (α-FeOOH) and akageneite (β-FeOOH) components of S1 and S2. Thus, starch functionalization changed the bandgap, the band positions, and the two components relative band alignment.

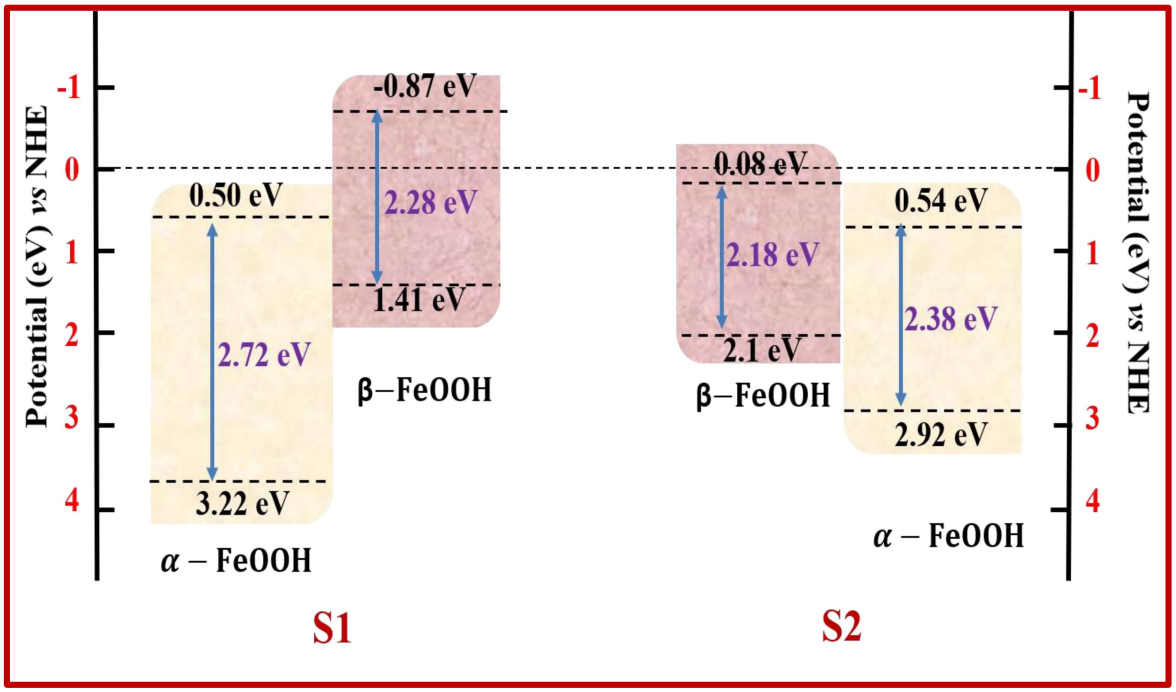

Figure 5.7 Band edges and band gap values of S1 and S2.

5.3.3 Fenton degradation of PNP by S1 and S2

Figures 5.8a and 5.8b show the change in PNP's UV-visible spectrums with time over S1 and S2, respectively. These plots were obtained under dark Fenton reaction conditions. Almost 10% of PNP got degraded over S1 in the investigated period (60 minutes). In contrast to this, about 50% of PNP degraded during the same time interval on S2. Therefore, S2 was a better Fenton catalyst for PNP degradation. It appears that starch functionalization altered the nature of the active sites on the iron oxyhydroxide nanocomposite, and this resulted in better Fenton catalytic properties. In other words, the differently coordinated surface sites of rice grain shaped starch functionalized

nanostructures led to the improvement of their Fenton catalytic activity [Cao *et al.* (2016)].

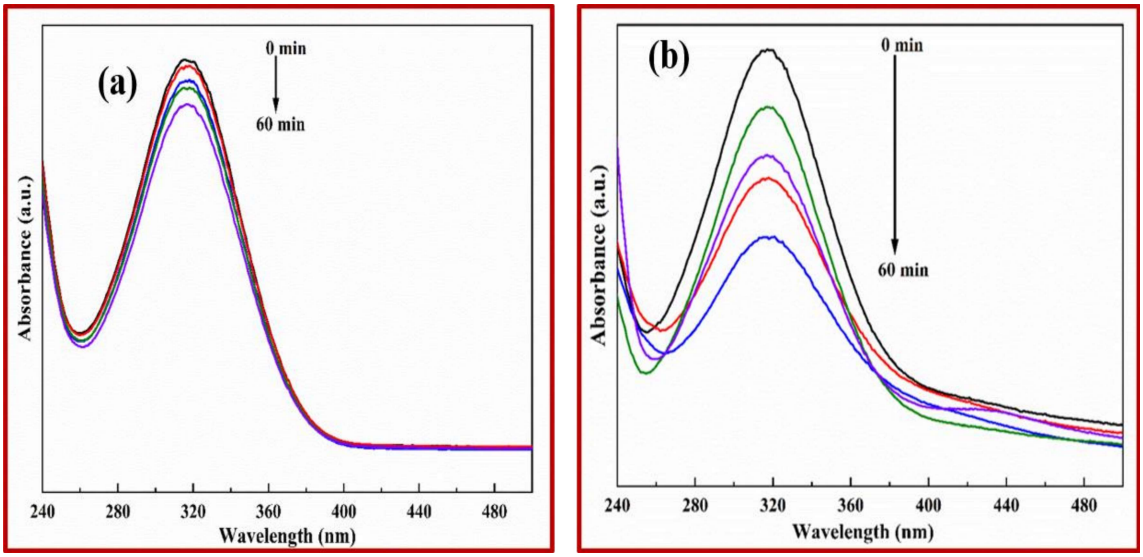

Figure 5.8 UV-visible plots of Fenton degradation (in the dark) of PNP at regular intervals of reaction time catalyzed by **(a)** S1 and **(b)** S2 samples.

5.3.4 Visible light photo-Fenton degradation of PNP over S1 and S2

Figure 5.9a and 5.9b display visible light photo-Fenton degradation of PNP over S1 and S2. The rate of PNP degradation on S1 under visible light was about four times observed in the absence of light. However, the visible light irradiation increased the PNP degradation rate drastically over S2. It was about twelve times that recorded in the dark (for S2). As described in section 4.3.3, the differential rate law equation was used to investigate the kinetics of PNP degradation by the photo-Fenton reaction.

The photodegradation of PNP catalyzed by S1 and S2 follows pseudo-zero order rate kinetics. Figure 5.9c presents $\left(\frac{A_t}{A_o}\right)$ against t plots for photo Fenton degradation of PNP on S1 and S2. Here A_o and A_t are the initial and final PNP concentrations at time t = 0 and t, respectively. Nearly perfect linear fits were obtained for both S2 and S1 catalytic samples. The S2 catalyzed PNP degradation kinetics was much faster. Pseudo zero-order

rate constant (k_{app}) was derived from the slope of the linear fits to the respective plot (Figure 5.9c). The S2 catalyzed k_{app} value is an order of magnitude higher than that for the reaction catalyzed by S1 (Table 5.1). However, the photocatalytic activities of different samples (S2 and S1) should not be compared using rate constants for several reasons.

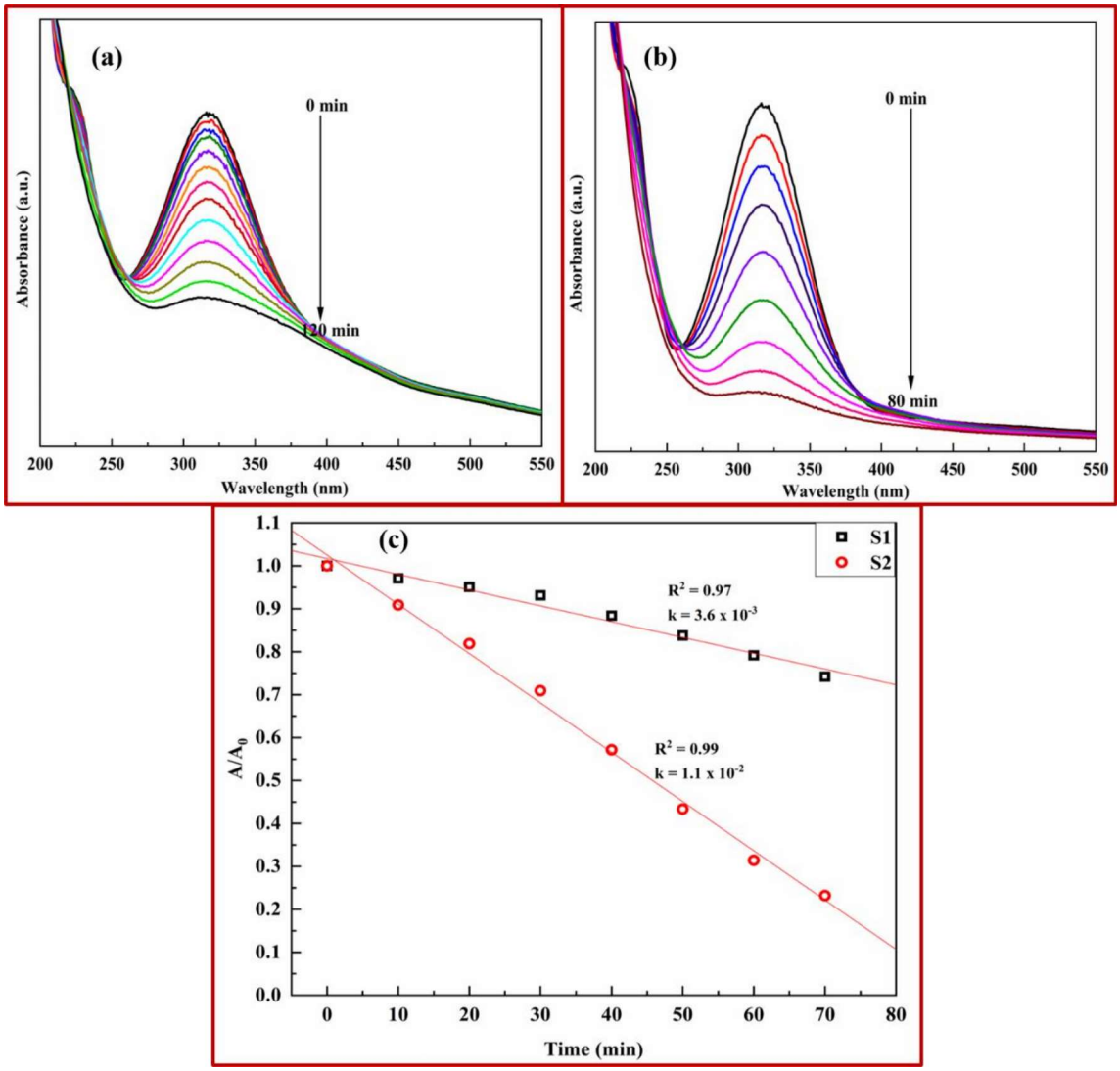

Figure 5.9 UV-visible plots of photo Fenton degradation of PNP at regular intervals of reaction time (under visible light conditions) catalyzed by **(a)** S1 and **(b)** S2 samples. **(c)** The plots of (A/A_0) [absorbance (A) measured at λ_{max} 317 nm] versus time for (PNP degradation) reactions catalyzed by S1 and S2.

First, for the same reaction catalyzed by different catalysts, the reaction's order may be different, rendering any comparison impossible. Furthermore, in the rate constant calculation, neither the amount of product formed nor the catalyst used is taken into

account. Therefore, in this study, the activities of the catalysts were measured in terms of TOF (calculated according to equation 4.4).

Table 5.1 compares the TOF values of photo-Fenton degradation of PNP under visible light catalyzed by S1 and S2 with those reported previously by other authors. However, the light sources used by the authors in these two ($SiO_2/Fe_3O_4/C@TiO_2$ and GO/Fe_2O_3) cases [Hou *et al.* (2016), Guo *et al.* (2013)] were of much higher intensity than that used for photo-Fenton degradation catalyzed by S2 or S1. Moreover, TiO_2 based catalysts require UV light for photocatalysis.

Table 5.1 Comparison of TOF values for Photo-Fenton degradation of PNP in the presence of different catalysts studied earlier in literature with ones investigated in this work.

Catalyst	**Light Source**	**TOF (moles gram^{-1} min^{-1}**	**Reference**
S1	Cool white LED (0.1470 W/cm^2, visible range light source)	5.04 x 10^{-6}	This work
S2	Cool white LED (0.1470 W/cm^2, visible range light source)	8.36 x 10^{-6}	This work
$SiO_2/Fe_3O_4/C@TiO_2$	UV light from a Xenon lamp (CHFXQ 500 W)	5.65 x 10^{-6}	Hou *et al.* (2016)
CuO/Al_2O_3	Microwave irradiation of 100 W power	8.2 x10^{-7}	Pan *et al.* (2015)
$GO\text{-}Fe_2O_3$	300W Dy Lamp (420nm visible light source)	2.5 x 10^{-6}	Guo *et al.* (2013)

**The TOF values from publications by authors other than ours were calculated from the data given in literature using Eq. 4.*

Previous investigations in literature [Khatamian *et al.* (2012)] on heterogeneous Fenton degradation of PNP have reported that this oxidation occurs either by the formation of quinone or 4-nitrocatechol (4-NC) as intermediates. Later, both intermediates oxidize to aliphatic acids and finally to CO_2 and water. The formation of quinone intermediate would be indicated by a UV-vis peak to the left of the primary PNP absorption, while 4-NC displays an absorbance to the right. No absorption peaks were observed either on the left or right of the PNP absorbance peak Fig. 5.9, indicating the absence of intermediates with visible range absorbance. In other words, PNP was directly oxidized to aliphatic acids or smaller molecules.

5.3.5 Photo - Fenton degradation of MO by S1 and S2

Figure 5.10a and 5.10b present the UV-visible spectrums with time for aqueous MO solution (subjected to heterogeneous Fenton conditions in the dark) over S1 and S2, respectively. Negligible MO degradation took place under dark Fenton conditions over S1. Only 10% MO degradation was observed after 60 minutes in the S2 catalyzed Fenton reaction. Figure 5.11a and 5.11b display the UV-visible spectrums for photo-Fenton degradation of MO with time. In this case, the photo-Fenton MO degradation was much faster than the corresponding Fenton result with the same catalyst. The change was even more dramatic in the case of the photo Fenton reaction on S2. It was almost fifteen times faster than the corresponding response in the dark. Furthermore, all peaks decreased in intensity with time, suggesting MO degradation to small molecules having no UV-visible absorbances.

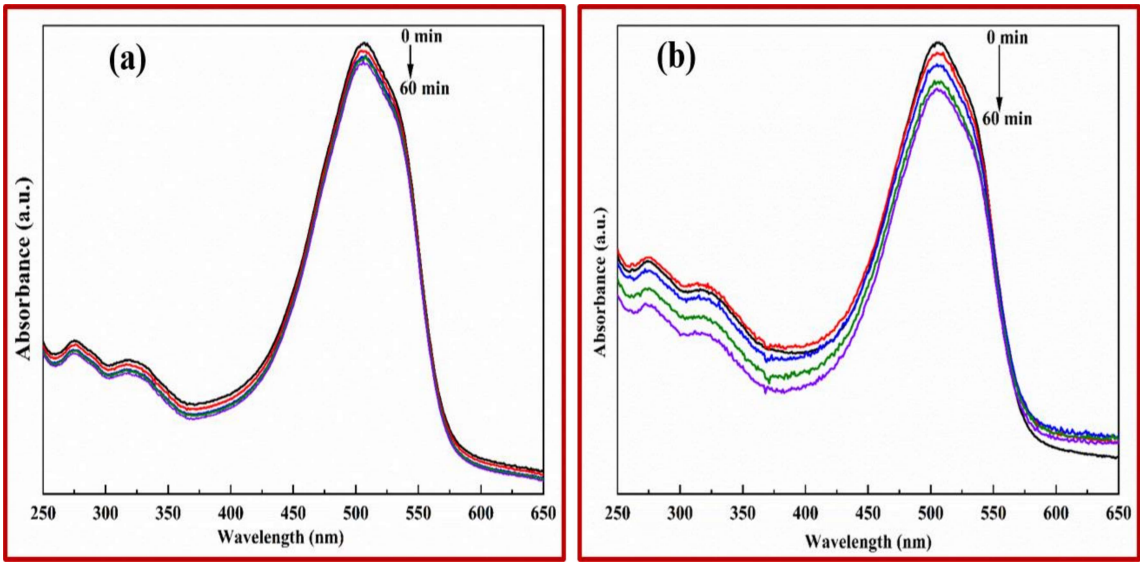

Figure 5.10 UV-Visible plots for the Fenton degradation of MO on **(a)** S1 and **(b)** S2 samples, respectively.

As mentioned in the preceding subsection, the order of reaction was first obtained by the differential rate law method (As described in section 4.3.3). The photo Fenton degradation of MO was found to follow zero-order rate kinetics. Then the rate constant was obtained from the slope of the A/A_0 versus time plots (Figure 5.11c). Here A and A_0 denote the absorbance of MO at time t and t_0, respectively. The rate constant of the photo Fenton reaction on S2 was higher than that over S1 (Table 5.2).

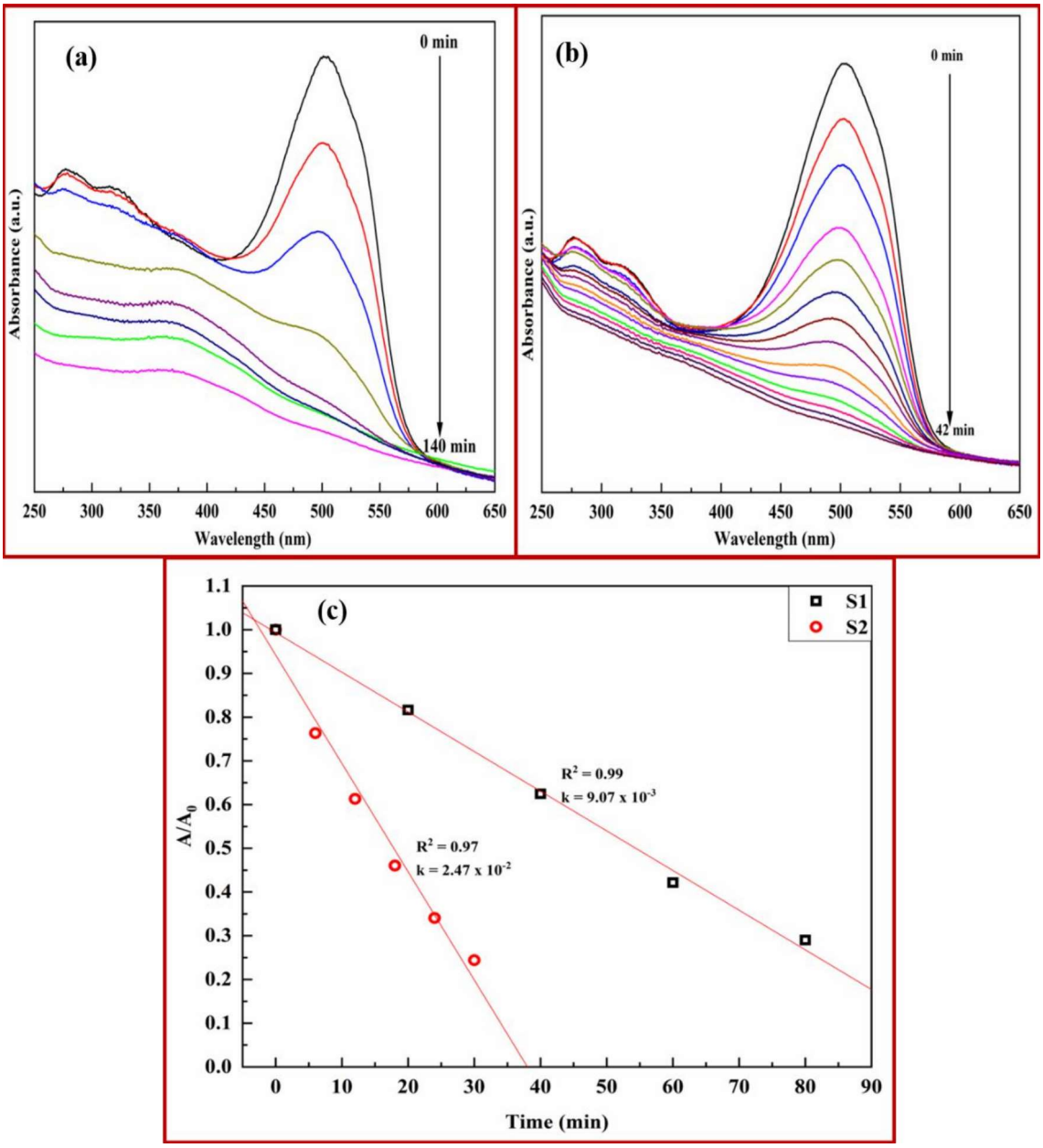

Figure 5.11 UV-Visible plot for the photodegradation of MO as a function ofreaction time under the optimum reaction conditions by **(a)** S1 and **(b)** S2 catalytic sample **(c)**Photo Fenton kinetics (A/A_0) [absorbance (A) measured at λ_{max} 506 nm] versus time plots of reactions carried over S2 and S1.

Table 5.2 Comparison of MO photodegradation TOF values on different nanocomposites studied earlier in literature with ones investigated in this work.

Catalyst	**Light Source**	**TOF (moles gram^{-1} min^{-1})**	**References**
S1	Cool white LED (0.1470 W/cm^2, visible range light source)	3.56 x 10^{-5}	This work
S2	Cool white LED (0.1470 W/cm^2, visible range light source)	1.26 x 10^{-4}	This work
TiO_2/ β-FeOOH	Visible light(500 W xenon lamp and UV light (Hg Lamp)	8.76 x 10^{-6}(VL) 9.88 x 10^{-6} (UV)	Xu *et al.* (2013)
Fe_2O_3-SiO_2	1000 W tungsten-halide lamp (Philips) equipped with wavelength cutoff filters (λ> 420 nm)	1.97 x 10^{-6}	Zhou *et al.* (2018)
α-FeOOH QDS/g-C_3N_4	500 W Xe lamp with UV cutoff filter (> 420 nm)	5.09 x 10^{-5}	Qian *et al.* (2018)
Fe_2O_3/Au/SiO_2	300-W xenon lamp with a filter (λ>420 nm)	1.52 × 10^{-6}	Xiao *et al.* (2019)

Table 5.2 compares TOF values of photo-Fenton degradation of MO under visible light catalyzed by S1 and S2 with those reported previously by other authors. As mentioned earlier, rate constants published in different studies may not be comparable, and TOF values are more appropriate for comparing different systems. Table 5.2 gives this information about the TOF values for photo Fenton degradation of MO catalyzed by iron oxyhydroxide nanocomposites. The S2 photocatalyst demonstrated much better

photo-Fenton results. The TOF value obtained was about three orders of magnitude faster than those reported by other researchers.

5.3.6 Recyclability test

Recyclability test (figure 5.12) performance evaluated the stability of the S2 nanocomposite in the photocatalytic reaction. The S2 nanocomposite showed good catalytic activity even after the 5th run.

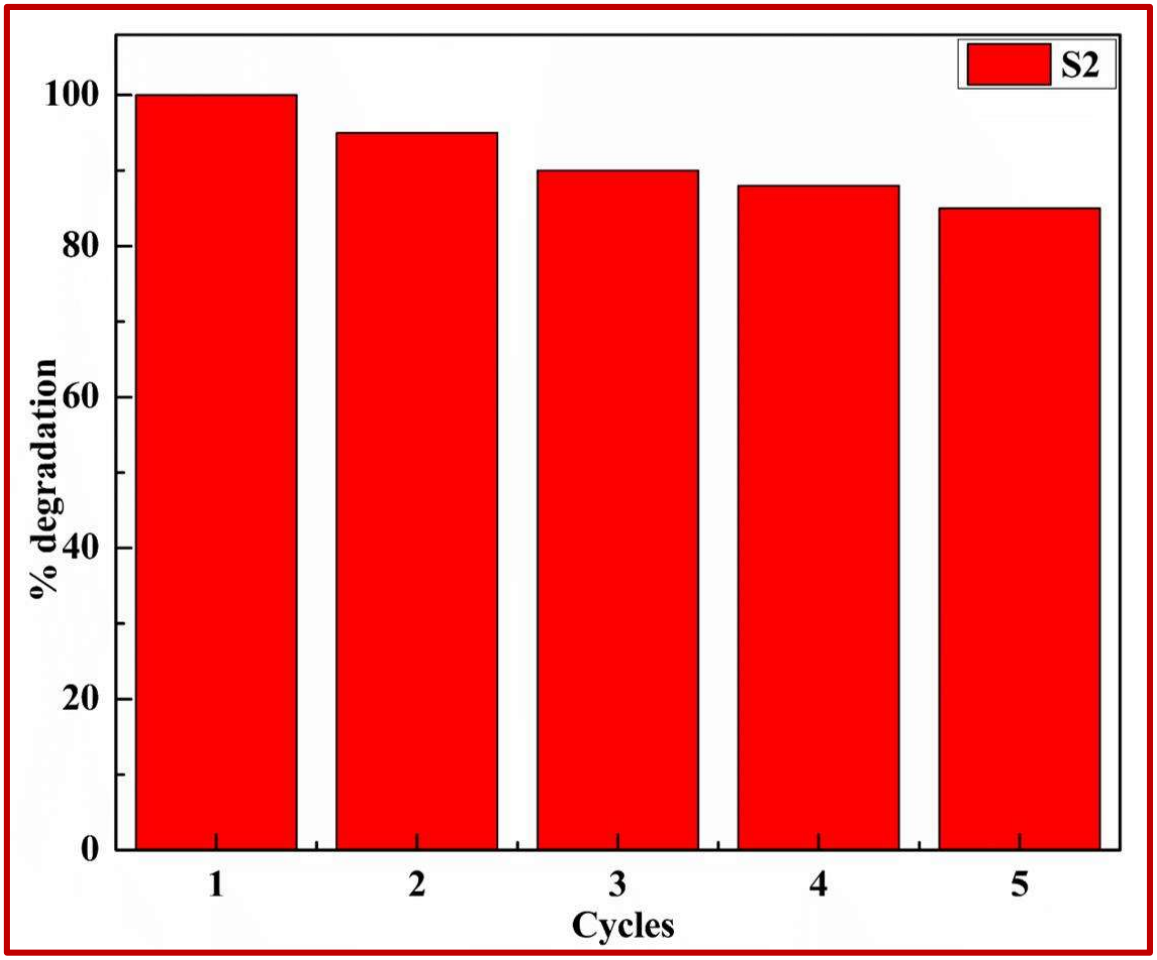

Figure 5.12 Five cycles of S2 reusability for PNP degradation reaction.

5.3.7 Photocatalytic mechanism

This section proposes a plausible mechanism to explain the improved photocatalytic properties of S2. This mechanism's premise is the experimental facts presented in this chapter and other workers' previously published research. Starch functionalization of iron

oxyhydroxide nanocomposites improved their heterogeneous Fenton as well as photo Fenton catalytic properties. Enhanced Fenton properties (in the dark) due to functionalization means that it changed the active site's nature on the catalyst. Such an improvement could be because of a change in the electronic state of the active site. Another reason could be the better adsorption properties of S2. The smaller bandgap of goethite and akageneite phases in S2 compared to S1 affirmed the change in the nanomaterial's electronic structure.

The significantly higher photocatalytic efficiencies resulted from the combination of the reduced bandgap and enhanced charge separation as proposed in the schematic (Figure 5.13). The iron oxyhydroxide particles were nanocomposites of goethite and akageneite. The band positions of goethite and akageneite are staggered relative to each other [Jelle *et al.* (2016)]. Thus, on visible light irradiation, adjacent iron oxyhydroxide phases (goethite and akageneite) got photo-excited. Following the p-n mechanism, the excited electrons migrated from akageneite CB to goethite CB, while holes from the goethite VB moved to the akageneite VB. As a result, holes accumulated on the VB of akageneite, while electrons were mainly on the goethite CB. The oxidation of hydrogen peroxide to peroxyl radical occurred on the VB of akageneite, while electrons on the goethite CB reduced hydrogen peroxide to form hydroxyl radicals.

The goethite CB is nearly in the same position in S1 and S2; the kinetics of H_2O_2 reduction should be almost the same due to both nanocomposites. However, the VB edge of akageneite in S2 is significantly more positive (~2.1 eV) than S1 (~1.41 eV). The more positive akageneite VB of S2 gives enhanced H_2O_2 to hydroperoxyl radical oxidation. Hence, besides better hydrophilicity, the altered VB position appears to be the main reason for the improved photocatalytic properties of S2.

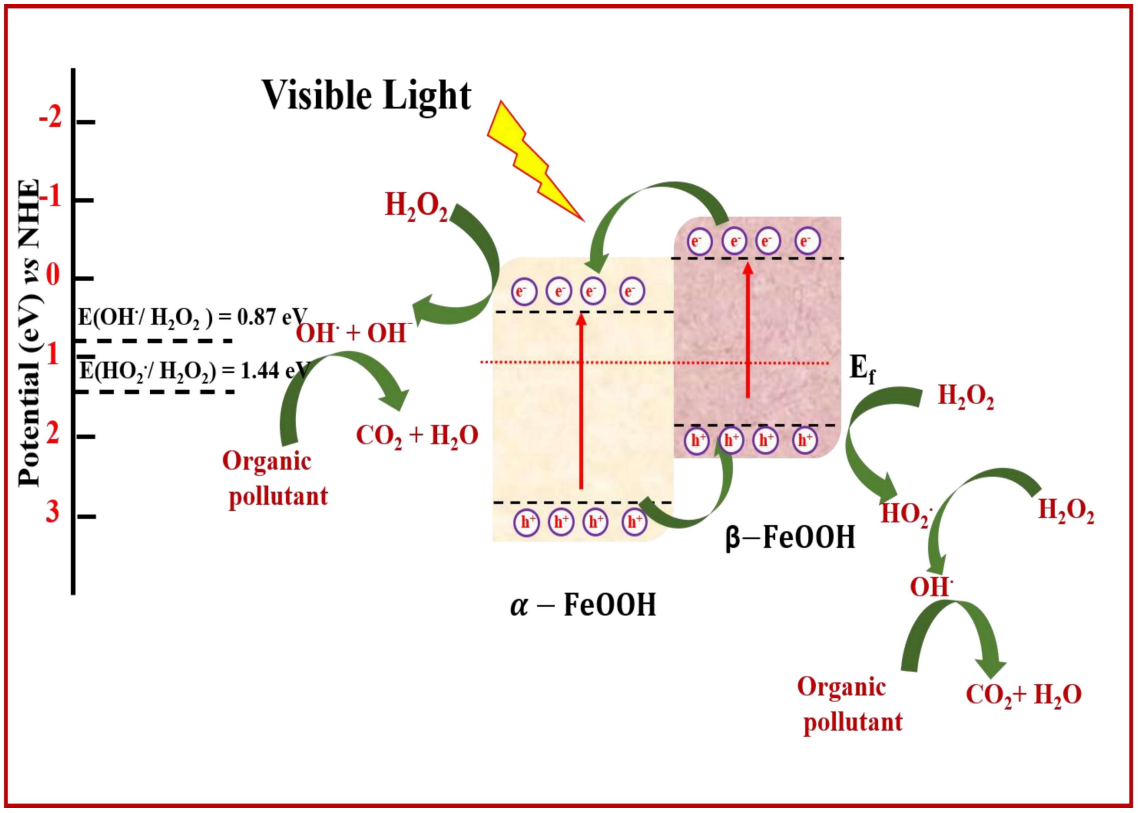

Figure 5.13 Schematic representation of the mechanism proposed for explaining the photo- Fenton degradation of organic pollutants.

5.4 Conclusions

A green synthesis methodology gave rod-shaped nanocomposites of goethite and akageneite. Starch functionalization resulted in rice-shaped nanocomposite particles (S2) with the same phase composition but increased hydrophilicity. Both Fenton and photo Fenton efficiencies for PNP and MO oxidation increased on starch functionalization. An increase in (dark) Fenton reaction activity of S2 suggested that starch surface modification alters the active sites. The latter was expected since rice like nanostructures has differently coordinated surface sites. Starch functionalized and non-functionalized nanocomposites were p-n heterojunctions of goethite and akageneite. The p-n charge separation mechanism led to the accumulation of electrons on the CB of goethite, while the holes got concentrated on the VB of akageneite part of these nanocomposites. The more positive

VB position of akageneite in S2 led to the enhanced photocatalytic performance of this nanocomposite.